Control of nitrogen insertion during the growth of nitrogen-containing carbon nanofibers on cordierite monoliths walls

Laura Roldán, Sabino Armenise, Yanila Marco, Enrique García-Bordejé*

Instituto de Carboquimica (C.S.I.C.), Miguel Luesma Castán 4, 50018 Zaragoza, Spain

Abstract

A well attached coating of nitrogen-functionalised carbon nanofibers (N-CNFs) have been prepared on the walls of cordierite monolith channels. It is formed *via* concurrent decomposition of ethane and ammonia catalysed by nickel nanoparticles dispersed on alumina coated cordierite monolith. N-CNF/monoliths synthesised employing several growth temperatures and NH_3 compositions were exhaustively characterised by Raman, XPS, elemental analysis and TEM. Synthesis conditions affected profoundly content and type of nitrogen functionality, enabling its fine tuning. N-CNFs surface chemistry and microstructure differed remarkably from its N-free counterparts.

1. Introduction

Carbon nanofibers (CNF) or carbon nanotubes (CNT) doped with nitrogen atoms have showed superior performance than their un-doped counterparts when used as catalyst support for different reactions. For instance, they have been used as Ru support for

---

* Corresponding author: Tel.:+ 34 976733977; fax.: +34 976733318 *E-mail address:* jegarcia@icb.csic.es

ammonia decomposition,[1,2] as Pt[3] or Fe[4] support for oxygen reduction reaction, as Pd support for direct synthesis of H_2O_2 from H_2 and O_2, [5] and for the hydrogenation of cynamaldehyde,[6] as Pd and Au support for the aerobic selective oxidation of alcohols[7] and for the preferential oxidation of CO.[8] Nitrogen containing CNF/CNT have also been used without any deposited metal as catalyst for alkane dehydrogenation, [9,10] as basic catalyst for Knoevenagel Condensation [11] or as electrocatalyst for oxygen reduction reaction.[9,12-17]

For practical applications, the immobilisation of CNF on structured reactor is highly desired because it has notable advantages compared to the operation using loose nanoscopic CNFs. To name a few, the catalyst is easier to separate, the pressure drop is lower and there is less tendency to plugging. Cordierite monoliths are a type of structured reactor, which is commercially available due to their wide use in automotive pollution control.[18] In previous works, we reported the immobilisation of a CNF coating on cordierite monoliths.[19] CNFs are usually functionalised with oxygenated surface groups to deposit the active phase in a dispersed fashion. Nitric acid is commonly employed to functionalise carbon nanofiber and carbon nanotubes with oxygenated surface groups. Nevertheless, this treatment affected negatively the attachment of CNF on cordierite monoliths.[20] In contrast, the treatments with H_2O_2 and diluted HNO_3 were not harmful for the adhesion of CNF but the degree of functionalisation was lower than using concentrated nitric acid.

To avoid the need of postfunctionalisation, nitrogen functionalisation has been carried out simultaneously to CNF growth. N-CNFs have been grown on cordierite monolith by concurrent decomposition of ethane and ammonia. A set of samples have been prepared by varying the growth temperature and C_2H_6: NH_3 ratio in the gas feed. The impact of these parameters on the CNF yield, microstructural morphology and nitrogen functionalisation has been elucidated by using several techniques such as XPS, Raman, elemental analysis and TEM.

2. Experimental

2.1. Catalyst preparation

Cordierite monoliths (from Corning, 1 cm diameter, 5 cm length, 400 cpsi) were washcoated with alumina by a dip-coating method similar to the sol-gel coating described by Nijhuis et al.[21] In this method, a sol is prepared from pseudoboehmite (AlOOH, Pural from Sasol), urea and 0.3 M nitric acid with a weight ratio of 2:1:5. After stirring for 30 min, the dried monolith is dipped in this sol. The liquid inside the monolith channels is removed by flushing thoroughly with pressurized air and then dried at room temperature for 24 hours while continuously being rotated around its axis. Finally, the monolith is calcined in air at a rate of 1 K/min up to 873 K to obtain the γ-alumina washcoating.

Nickel was deposited by adsorption from a pH-neutral nickel solution as described elsewhere.[22] 29 g $Ni(NO_3)_2 \cdot 6\ H_2O$ (pure, Sigma-Aldrich), 80 g NH_4NO_3 (pure, Sigma-Aldrich) and 4 ml ammonia solution (25 %) were mixed in a 1 litre bottle. The monolith samples were kept overnight in this solution while continuously flowing liquid through the channels. Then the monoliths were rinsed thoroughly with deionised water, followed by drying first at room temperature overnight and later at 373 for 1 hour. Subsequently, the monoliths were calcined in flowing nitrogen (1 K/min) up to 873 K followed by a 2 hours dwell time.

2.2. Carbon nanofiber growth

The monolith was fitted in a quartz reactor by wrapping it in quartz band. The reduction of the calcined catalyst was carried out in a hydrogen atmosphere at 823 K for 120 min (5K/min). The monolith was then heated (5 K/min) to the temperature of CNF-growth. The growth was carried out at several temperatures, *i.e.* 823, 873, 923, 973 and 1023 K, with a total flow of 100 ml/min of C_2H_6:NH_3 gas mixture of different compositions (v/v), namely (100:0), (90:10), (75:25), (62,5:37,5), (50:50), (37,5:62,5), (25:75), (10:90). The CNF growth is allowed to proceed for 3 hours following up by cooling down in inert atmosphere. This growth time is long enough for the catalyst been deactivated due to encapsulating carbon, as corroborated by gas chromatography analysis of the flue gas and TEM.

The samples have been named as CNF*X*A*Y,* where *X* and *Y* are numbers that denote the percentage of NH_3 in the gas feed and the temperature at which the growth of CNFs has been carried out, respectively. The A between *X* and *Y* stands for ammonia.

2.3. Characterisation

Raman characterisation was performed in a Horiba Jobin Yvon, LabRAM HR UV-VIS NIR. Raman spectra were recorded with an Ar-ion laser beam at an exciting radiation wavelength of 532 nm. The intensity of the D and G bands was measured from the maximum height of the peaks after subtracting the baseline.

XPS spectra were recorded with an ESCAPlus Omnicrom system equipped with a Al Kα radiation source to excite the sample. Calibration of the instrument was done with Ag $3d_{5/2}$ line at 368.27eV. All measurements were performed under UHV, better than 10^{-10} Torr. Internal referencing of spectrometer energies was made using the dominating C 1*s* peak of the support at 284.6 eV and Al 2*p*, at 74.3eV. The program used to do curve fitting of the spectra was XPS CASA routines after baseline Shirley method.

Transmission electron microscopy (TEM) investigation was performed with JEOL-2000 FXII electron microscope equipped with a field emission gun. Coupled there is a system for energy analysis of dispersed X-rays INCA 200 X-Sight de Oxford Instruments with resolution of 136 eV a 5.9 KeV, which allows the determination of the chemical composition in the focalized micro-region. TEM specimens were prepared by ultrasonic dispersion in ethanol of powder retrieved from the monoliths. A drop of the suspension was applied to a holey carbon support grid.

The adhesion of N-CNF to monoliths was checked by ultrasonic test. After drying the monolith at 120 ºC for 1 hour, it is weighted and introduced in a beaker with ethanol. Subsequently, the beaker is introduced in ultrasonic bath (frequency 40 KHz) and it is kept during 15 minutes. After drying at 120 ºC during 1 hour, the monolith is weighted. Form the difference between the initial and final weight, the coating weight loss is calculated.

3. Results and discussion

3.1. Influence of synthesis parameters on carbon yield and nitrogen content determined by elemental analysis

C_2H_6 and NH_3 are decomposed by Ni nanoparticles according to the global equations 1 and 2, respectively. Several carbon atoms produced by equation 1 bond together to form graphitic planes. These planes adopt the form of nanotubes or nanofibers, depending on the synthesis conditions and the properties of the catalyst. When NH_3 is fed together with C_2H_6, reaction 2 also takes place and the produced N atoms bonds to C atoms, introducing distortions in the graphitic lattice. It can be envisaged that different synthesis conditions, such as temperatures or compositions, should affect kinetics and thermodynamics of each reaction in a different way, ending up in N-CNFs with a variety of functionalisations.

$$C_2H_6 \rightarrow 2\,C + 3H_2 \qquad (1)$$

$$2NH_3 \rightarrow 2N + 3H_2 \qquad (2)$$

N-CNF/monoliths were prepared employing different conditions of temperature (823-1023 K) and NH_3 composition in the gas feed (0-90%). The carbon and nitrogen content of each sample was measured by elemental analysis. The effect of temperature and NH_3 composition on CNF yield and nitrogen content is reflected in the 3-D diagrams of figure 1 and 2, respectively. The maximum attained N/C ratio in this work was about 12.8 wt%, which is comparable to those prepared *via* one-step synthesis using nucleobases as precursors[23] or *via* postfunctionalisation.[24] This N content is moderate since it is reported that MWCNT can reach average concentrations 15-20 at%.[25,26] However, very high nitrogen content is not needed depending on the application because it can be detrimental for electric conductivity.[27]

For NH_3 concentrations below 60%, the N-CNF loading increases as the growth temperature rises in agreement with an activated catalytic process. Likewise, the maximum carbon yield is found for the highest temperature (1023 K). In contrast, for NH_3 concentrations above 60%, the maximum productivity is not found for the highest temperature used but for a temperature slightly lower, *ca*. 973 K. The dependence of N-CNF loading on inlet NH_3 concentration exhibits a maximum at values between 30-40 % NH_3. This could be rationalized because certain amount of NH_3 in the feed is beneficial to prolong catalyst lifetime because it prevents its encapsulation by carbon.

However, NH_3 concentration exceeding a certain value, *ca*. 40%, decreases the carbon productivity. Elsewhere, it has been reported that nanotube growth terminates if the nitrogen feed rate is too large.[28] This can be attributed to nitrogen blocking the adsorption sites on the catalyst. In addition, carbon input is not sufficient when using low C_2H_6 concentrations, slowing down and eventually stopping the growth. Another possibility is that NH_3 promotes the production of active species ($NH_2\cdot$, H_2) which compete with sp^2 carbon formation (etching effect).[29,30]

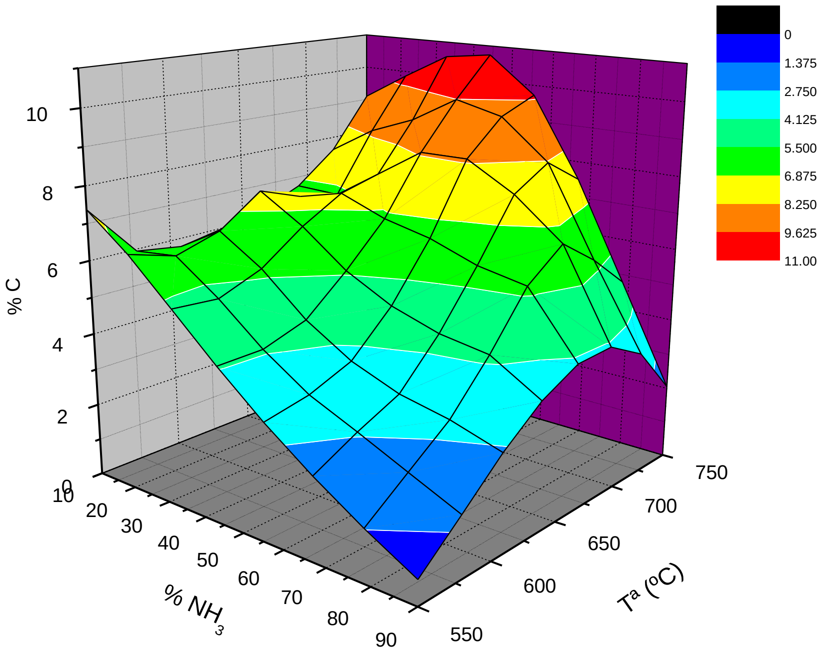

Figure1. N-CNF loading on monoliths determined by elemental analysis as a function of the growth temperature and NH_3 percentage in the gas feed (ethane to balance)

The degree of nitrogen incorporation within CNFs (figure 2) exhibits a maximum for intermediate synthesis temperatures at 873-923 K. Other researchers also found a N/C maximum at similar temperatures.[6] For the lowest temperature range, NH_3 decomposition kinetics is relatively slow, giving rise to marginal N incorporation into the graphitic lattice. On the other hand, for the highest temperature range, the higher bonding energy of the C-C bond compared to the C-N bond favors the formation of C-C and N_2 rather than C-N bond formation.[31] In contrast, CNFs synthesized at intermediate temperatures, *i.e.* 873-923 K, have less in-plane graphitic order than those synthesized at higher temperatures, which enhances nitrogen insertion within the graphitic lattice.

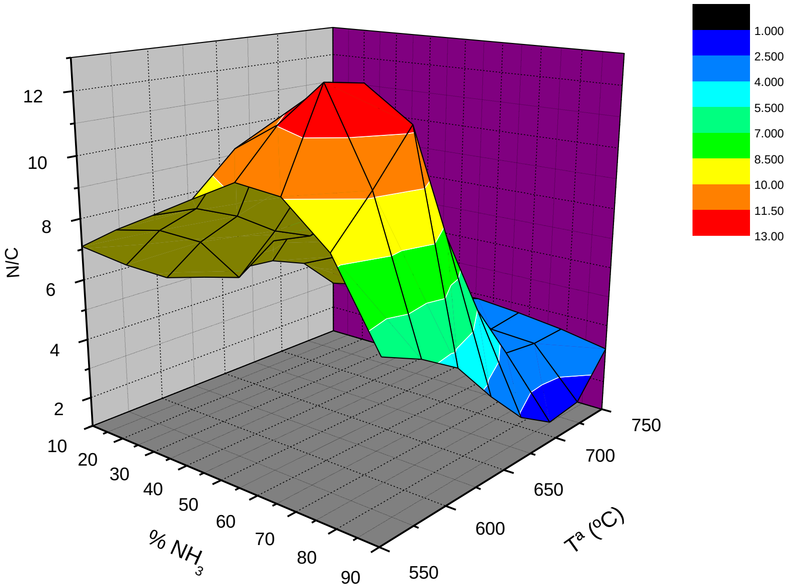

Figure 2. N/C percentage determined by elemental analysis as a function of the growth temperature and percentage of NH_3 in the gas feed (ethane to balance).

3.2. Characterisation of nitrogen-containing CNFs by microscopy and spectroscopy

SEM characterisation (not shown) revealed that the monolith channels are evenly coated by a layer of entangled N-containing CNFs. For CNF microstructure comparison, figure 3 show some representative TEM images of nitrogen-free CNFs (*a*,*b*) and N-containing CNFs (*c*,*d*). N-containing CNFs (figure 3*c*) are shorter and more curved than N-free CNFs (figure 3*a*). Nitrogen introduces defects in the graphitic planes which facilitate the bending of CNFs. This led to the formation of elbows as those observed in figure 3*c*. In both cases the samples are of the fishbone type with the graphitic planes forming an angle with respect to the CNF axis. This angle is smaller for the N-containing CNFs. Furthermore, N-containing CNFs have an inner hollow space separated regularly in compartments, unlike the nitrogen-free CNFs which are solid. Morphology of N-containing CNFs resembles stacked cups, in agreement with results reported in the literature.[2,32] These compartments became more pronounced when the diameter of inner tube is smaller, *i.e.* below 8 nm (see thinner CNF in figure 3*d*). In essence, adding NH_3 to the feed changes dramatically the microstructural morphology of the CNFs, graphitic planes are disposed more parallel to the axis and exhibit an internal hollow space. This suggests that the growth mechanism, *i.e.* decomposition-diffusion-precipitation of C fragments in catalyst particles is slightly different when NH_3 is present and when it is absent. Since a decrease in carbon arrival rate at the nucleation sites occurs in the presence of NH_3, it can be speculated that this makes carbon surface diffusion the dominant diffusion pathway leading to an inner empty space.

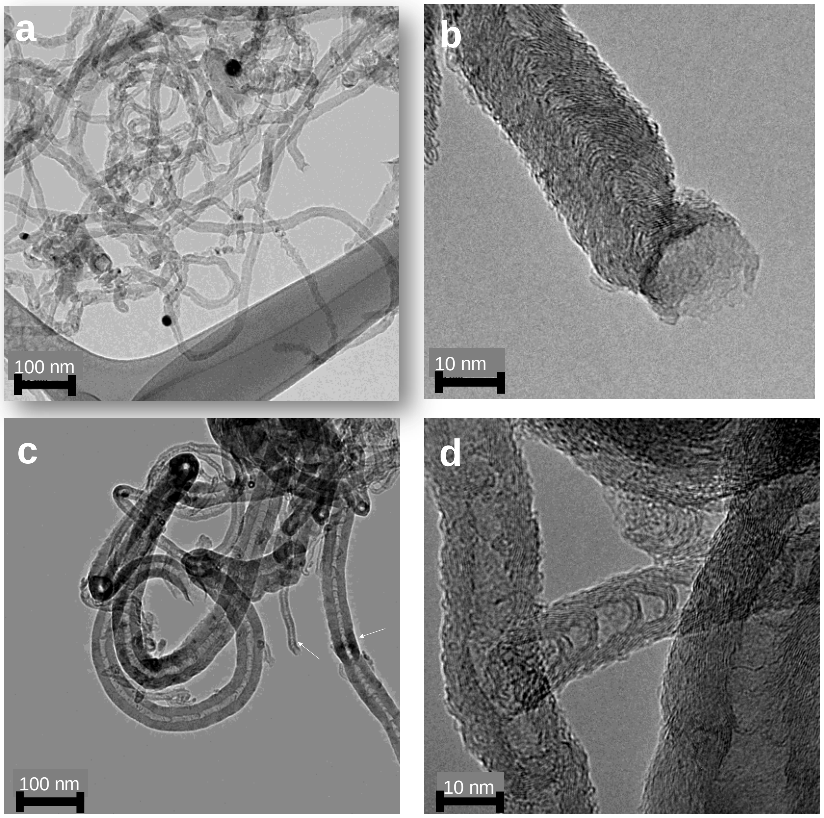

Figure 3. Representative TEM images of (a,b) N-free CNFs, which were grown at 873K using 50% H_2:C_2H_6 gas mixture; (c,d) N-containing CNFs, which were grown at 873K using 50% NH_3:C_2H_6 gas mixture.

Surface chemistry of the N-containing CNF/monoliths was characterized spectroscopically using Raman and XPS. Raman spectroscopy is a powerful tool to evaluate quantitatively the structural defectiveness caused by nitrogen incorporation within graphitic planes. The analysis of the peak positions and intensities gives information about changes of structural characteristics, namely graphite layer defectiveness.

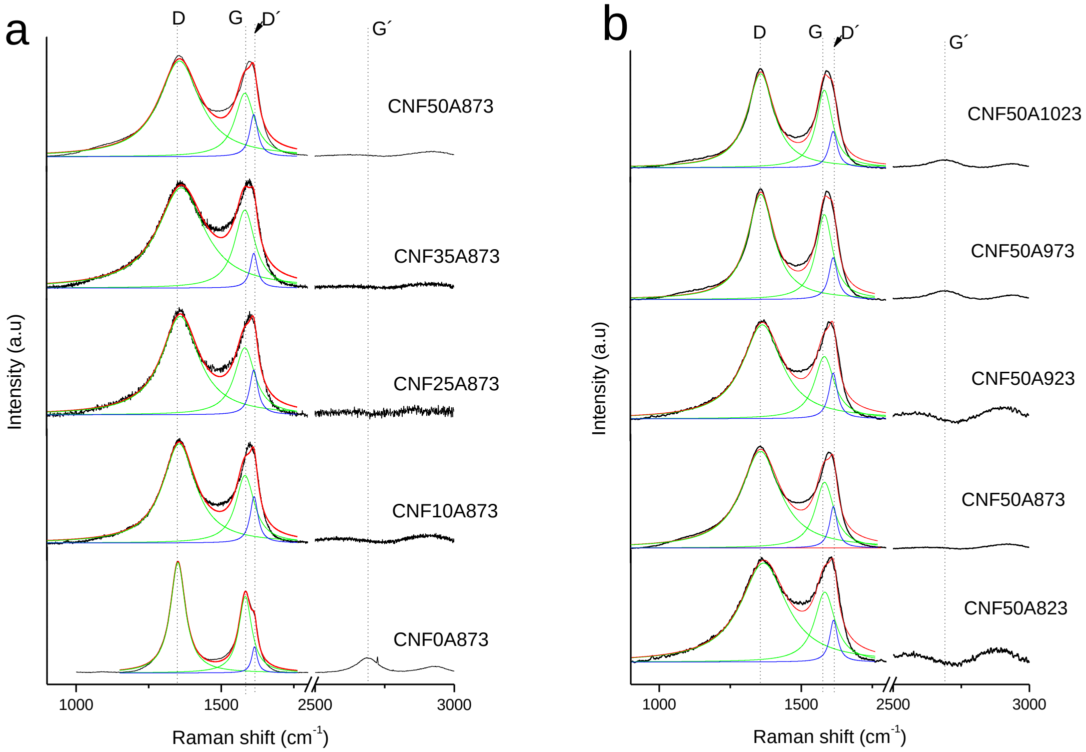

Figure 4. Deconvoluted Raman spectra for several CNF/cordierite monoliths. (a) CNF grown employing several NH_3 compositions in the gas feed at a constant temperature of 873 K ; (b) CNFs grown at different temperatures using a constant concentration of 50 % $NH_{\cdot 3}$ in C_2H_6.

Figure 4 *a,b* show the raman spectra of samples grown varying the NH_3 composition and temperature, respectively. The quantification is displayed in table 1. Nitrogen-free CNF/ monoliths (CNF0A873 in figure 4*a*) exhibit two strong peaks near 1351 and 1583 cm^{-1}, corresponding to the D- and G-bands, respectively. The G-band indicates the presence of crystalline graphitic carbon, whereas the D-band is attributed to disorders in the graphite structure. The G band shows a shoulder at 1614 cm^{-1}, which corresponds to the D′-band caused by second-order Raman scattering from the variation of the D-band.

The maximum of both D and G bands exhibited a blue shift for N-containing CNF/monolith compared to the N-free counterpart. The D-band upshifted up to 13 cm^{-1} from CNF0A873 to CNF37A873 sample (table 1). Kyotani and co-workers observed also an upwards displacement of D-band for N-doped CNFs.[23] They claimed that this was caused by the introduction of new disorder associated to the modification of fine structure due to nitrogen incorporation. The maximum of the combined G+D′ peak exhibits also a blue shift from 1583 cm^{-1} for N-free CNFs to 1601 cm^{-1} for N-containing CNFs. This shifting can be attributed to the increasing contribution of D′-band to the combined G+D′ peak as the nitrogen content increases. In addition, a significant broadening of D band occurs for the N-containing samples with respect to its N-free counterpart. The band width (FWHM) increases from 62.5 cm^{-1} for CNF0A873 up to more than 100 cm^{-1} for N-containing CNFs. The broadening of D-band upon nitrogen incorporation within graphite lattice has been also observed by other researchers,[33,34] even with minor amounts of nitrogen.

The intensity ratio of the two bands I_D/I_G is commonly used as an indicator of the degree of disorder within the graphitic lattice.[35] Some authors disregard the D′ band, considering as G band what is really a peak resulting from the combination of both G and D′ bands. This can lead to the wrong conclusion that the I_D/I_G ratio of N-containing CNFs is smaller that that of its N-free counterpart.[33] This conflicts with the general statement that the decrease of the I_D/I_G ratio is usually an indicator of improved in-plane order.[35] Here, we fitted the Raman spectra to three lorentzian functions corresponding to D, G and D′ bands, which resulted in a correlation coefficient of 0.99 (figure 4). The positions of G and D′ bands were constrained to the same positions as for the N-free CNFs since no shoulder ascribable to D′ was discerned for N-CNFs. After fitting the curves to these three bands, the I_D/I_G ratio correlates reasonable well with the CNF nitrogen content (figure 5). There is some scattering which can be attributed to the fact that some CNFs included in figure 5 have been grown using different temperatures. A higher growth temperature increases graphitic lattice order, which also contributes to descend the I_D/I_G ratio. For instance, samples grown at 973 K and 1023 K are below the average trend of those grown at 873 K. A further confirmation of the decrease of long-range order for N-doped CNFs is the absence of the G′ resonant Raman band at ~2700 cm^{-1}. This G′-band is only found for N-free sample (CNF0A873 in figure 4*a*) and in N-containing samples grown at temperatures above 973 K (figure 4*b*), which have the lowest N content and more graphitic character. An additional difference between CNF0A873 and N-CNFs is a larger G+D′ bandwidth for the N-containing CNFs (table 1).

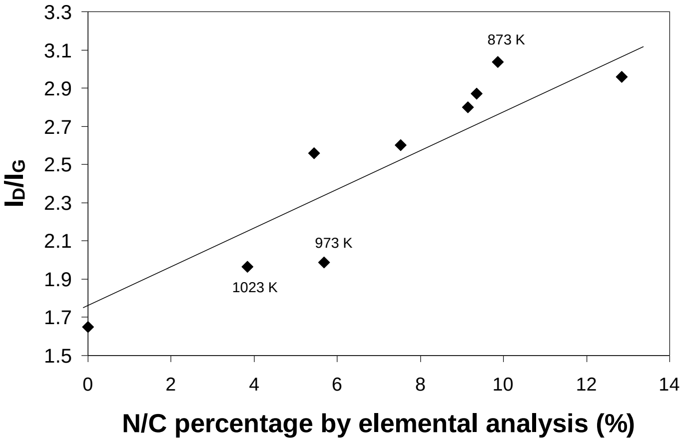

Figure 5. I_D/I_G ratio as a function of the N/C percentage measured by elemental analysis. The intensity of the D and G bands was determined after deconvolution of Raman spectra shown in figure 4.

Table 1. Raman parameters determined from figure 4

				D band		G band		
sample	NH_3 feed %	Growth Temperature K	N/C* %	position	FWHM	G+D′ position	FWHM	I_D/I_G
CNF0A873	0	873	0	1351	62.5	1583	54	1.65
CNF10A873	10	873	5.44	1356	138	1600	78	2.56
CNF25A873	25	873	7.52	1360	155	1601	86	2.60
CNF37A873	37	873	9.15	1364	194	1601	85	2.80
CNF50A873	50	873	12.84	1357	170	1601	82	2.96
CNF50A823	50	823	9.86	1367	195	1601	87	3.02
CNF50A923	50	923	9.35	1364	168	1600	68	2.88
CNF50A973	50	973	5.68	1359	114	1592	69	1.98
CNF50A1023	50	1023	3.84	1359	114	1590	61	1.96

*****measured by elemental analysis

Figure 6 *a* and *b* shows the deconvoluted XPS N1*s* spectra of N-containing CNFs grown at 873 K using different NH_3 composition and different temperatures, respectively. N1*s* spectra were calibrated *versus* the C1*s* peak, which is generally set to be at 284.6 eV. Four binding regions can be assigned to different nitrogen bonding of model carbonaceous materials.[14,36-40] These XPS peaks could be assigned to *(i)* pyridinic nitrogen (N1, 398.2–398.8 eV), which contain nitrogen atoms bound to two carbon atoms located at the edges or defect sites of graphene and contributes to the π system with one p-electron; *(ii)* pyrrolic, in which the sp^2-hybridized nitrogen is part of a five-member ring structure, or lactam groups (N2, 400.1–400.5 eV); *(iii)* quaternary nitrogen atoms (N3, 401.3–401.9 eV), including protonated pyridine or graphitic nitrogen,[38] where the nitrogen atom is incorporated into the graphene layer substituting a carbon atom; *(iv)* nitrogen oxide species and/or intercalated nitrogen molecules (N4, 404.0–405 eV).[38,41] The last peak was also referred to a π–π* shake-up satellite peak.[42,43]

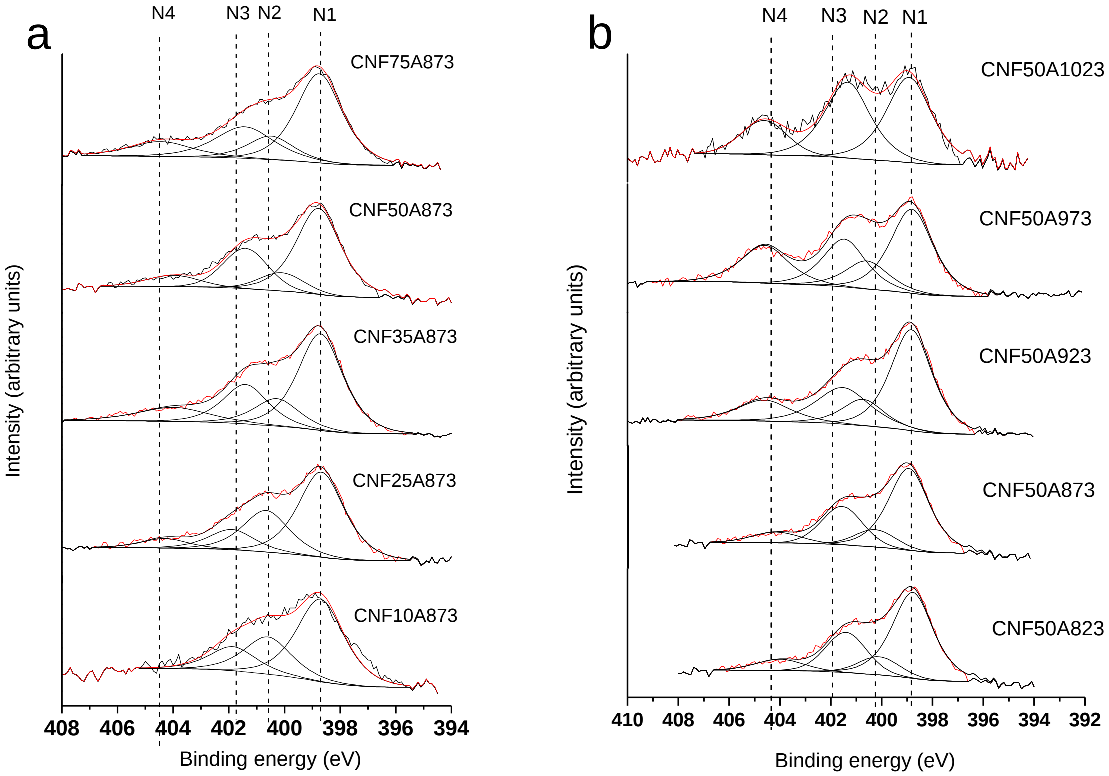

Figure 6. Deconvolution of N1*s* peak in XPS spectra of N-CNF grown at several conditions: (a) N-CNF grown using different NH_3 composition in the gas feed at a constant temperature of 873 K ; (b) N-CNFs grown at several temperatures using a constant $NH_{\cdot 3}$ concentration of 50 % in ethane.

Figure 7 shows the intensity of each nitrogen type as a function of the growth temperature. N1 peak intensity decays and N4 peak intensity increases as the growth temperature rises. N1 peak is ascribed to pyridinic nitrogen and N4 peak could be ascribed either to pyridine oxide or intercalated N_2. Since pyridine oxide is unlikely to be produced under the strict reducing conditions of CNF growth, N4 peak should be attributed to N_2 intercalated. N_2 formed by NH_3 decomposition can be retained in the inner hollow space of the CNFs as reported previously for N-containing CNTs.[32] N_2 formation is favoured at increasing temperatures, which would account for the increase of N4 peak as growth temperature rises. The proportion of nitrogen groups denoted as N2 and N3 remain almost constant until 973 K. For higher temperature (1023 K), quaternary nitrogen (N3) increases substantially at the expense of pyridinic (N1) and pyrrole (N2).

Table 2. Parameters determined by analysis of XPS spectra in figure 6

sample	N/C a.e %	N/C XPS %	Peak N1 398.2-398.8 %	Peak N2 400.1-400.5 %	Peak N3 401.3-401.9 %	Peak N4 404.0-404.7 %
CNF10A873	5.44	4.0	57.4	25.9	16.7	0.0
CNF25A873	7.52	5.9	53.8	17.6	21.3	7.3
CNF37A873	9.15	6.2	52.1	14.8	21.2	11.8
CNF50A873	12.84	7.4	52.5	14.4	25.2	7.8
CNF50A823	9.86	5.0	56.2	11.1	24.6	8.0
CNF50A923	9.35	4.38	50.25	13.14	23.37	13.25
CNF50A973	5.68	2.6	41.8	13.9	20.6	23.7
CNF50A1023	3.84	1.34	38.98	0.0	34.66	26.36

Figures 8 and 9 compare the N/C ratio values measured by both elemental analysis and XPS of N-CNFs grown varying the NH_3 composition and temperature, respectively. The

N/C ratio measured by XPS and elemental analysis follow similar trends. However, those values determined by XPS are always smaller than those determined by elemental analysis. This seems to indicate that CNF surface has lower nitrogen content than the internal part, since XPS measures the outermost surface. The difference between XPS and elemental analysis determinations should be more remarkable for the case of thicker N-CNFs. The higher N content at the CNF core would account for its higher curvature and the formation of graphene sheets crossing the inner hollow space. N4 type nitrogen is expected to be located also in the inner tube of the CNFs and XPS would not measure it for the CNFs of larger diameter. Figure 9 and 10 also illustrate the dependence of the pyridine/quaternary nitrogen ratio (right axis) as a function of the total nitrogen content. In general, this ratio decays slightly, *viz.* from 2.7 to 2.0, as nitrogen content increases due to increasing NH_3 feed concentrations (figure 8). N1/N3 variation is more remarkable as growth temperature increases, decaying from 2.3 to 1.1 (figure 9). Therefore it is possible to prepare samples with similar N contents but very different N1/N3 ratios by the interplay between NH_3 feed composition and growth temperature. N1 and N3 nitrogen types are the predominant groups and they are reported to be endowed with catalytic activity. For instance, the debate is open if the active phase for oxygen reduction reaction (ORR) is either pyridinic[44] or quaternary nitrogen.[45,46]

Similar dependence of nitrogen content and state on N-CNF synthesis conditions from hydrocarbon-ammonia mixtures has been reported elsewhere.[29] Nevertheless, as far as we know, there is no report about the preparation of N-CNF on a macrostructured support such as the monoliths used here. The monolithic form can supply benefits in terms of easy separation, low pressure drop and less plugging for several applications

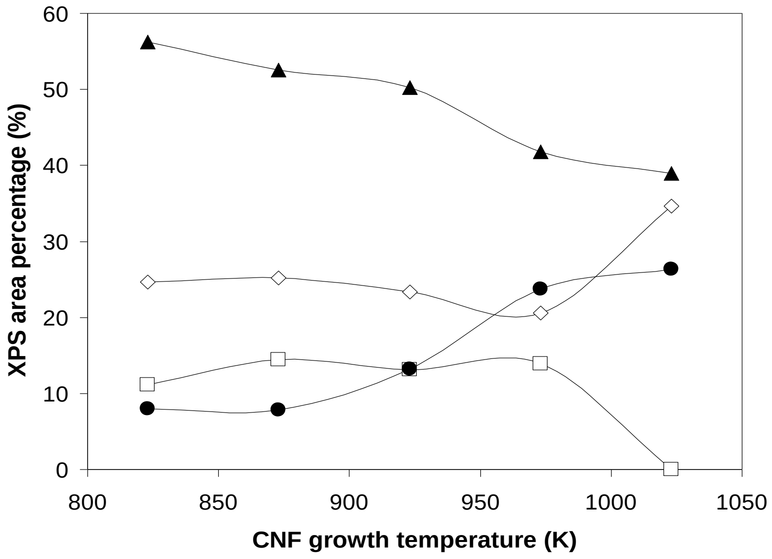

Figure 7. Contribution to XPS of different deconvoluted 1N*s* peak peaks in figure 5 as a function of the growth temperature: (▲) N*1*, pyridinic nitrogen (398.2–398.8 eV); (☐) N*2*, pyrrolic (400.1–400.5 eV); (◇) N*3*, quaternary nitrogen (401.3-401.9 eV); (●) N*4*, intercalated N_2 (404.0–405 eV).

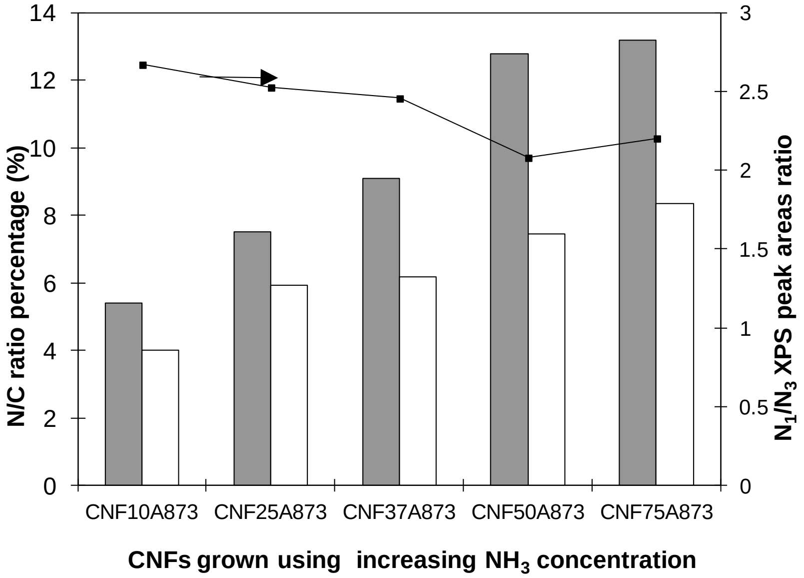

Figure 8. Left Y-axis, comparison of N/C ratio percentage determined by elemental

analysis (grey bars) and that determined by XPS (white bars) for N-CNF/monoliths prepared using increasing NH_3 concentrations and keeping temperature constant at 873 K ; Right Y-axis, ratio of N*1*/N*3* XPS peaks.

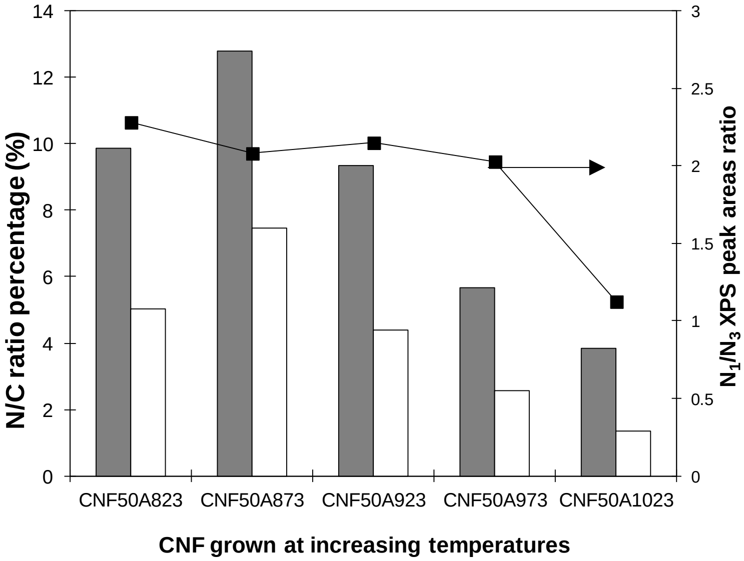

Figure 9. Left Y-axis, comparison of N/C ratio percentage determined by elemental analysis (grey bars) and that determined by XPS (white bars) for N-CNF/monoliths prepared using increasing growth temperatures and keeping constant NH_3 concentration at 50 %; Right Y-axis, ratio of N*1*/N*3* XPS peaks.

Conclusions

A layer of entangled nitrogen-functionalised CNFs have been coated on cordierite monolith walls. The incorporation of nitrogen functionalities to CNFs is conducted in one step, simultaneously to CNF growth. Therefore, it avoids post-synthesis functionalisation, which can be deleterious for the CNF layer attachment to the monolith besides increasing process cost.

The selection of the growth temperature and inlet NH_3 composition enables fine tuning the nitrogen content and prevailing type of nitrogen functionality, either pyridinic or graphitic. In essence, pyridinic nitrogen predominates for the lower growth temperature range (823-923 K), while the proportion of quaternary nitrogen increases for the higher temperature range (≈1023 K). The nitrogen content can be also varied from 0 to 12.8 wt% depending on the synthesis conditions. XPS measurement underestimates the total nitrogen content because CNF interior is more densely functionalised than its outer part. Structural disorder within graphitic planes is favoured when nitrogen contents rises or growth temperature decreases. The reproducibility of the synthesis opens the possibility for fundamental studies about the influence of content and type of nitrogen functionality on its behaviour as catalyst, catalyst support or electrocatalyst, where N-containing carbon nanofibers and nanotubes have shown remarkable performance. Furthermore, the monolithic form can supply benefits in terms of easy separation, low pressure drop and less plugging.

Acknowledgements

The authors are grateful to the financial support of the European Commission within the 7th FP (Grant agreement no.: 226347) and of Spanish Government (MAT 2008-02365).

Reference List

1. J. Chen; Z. H. Zhu; S. Wang; Q. Ma; V. Rudolph; G. Q. Lu *Chem. Eng. J.* 2010, **156** (2), 404.
2. F. R. García-García; J. Álvarez-Rodríguez; I. Rodríguez-Ramos; A. Guerrero-Ruiz *Carbon* 2010, **48** (1), 267.
3. C. H. Hsu; H. M. Wu; P. L. Kuo *Chem. Commun.* 2010, **46** (40), 7628.

4. G. C.-K. Liu; J. R. Dahn *Appl. Catal. A: Gen.* 2008, **347** (1), 43.
5. S. Abate; R. Arrigo; M. E. Schuster; S. Perathoner; G. Centi; A. Villa; D. Su; R. Schlögl *Catal. Tod.* 2010, **157** (1-4), 280.
6. K. Chizari; I. Janowska; M. Houllé; I. Florea; O. Ersen; T. Romero; P. Bernhardt; M. J. Ledoux; C. Pham-Huu *Appl. Catal. A: Gen.*2010, **380** (1-2), 72.
7. A. Villa; D. Wang; P. Spontoni; R. Arrigo; D. Su; L. Prati *Catal. Tod.* 2010, **157** (1-4), 89.
8. E. Castillejos; R. Chico; R. Bacsa; S. Coco; P. Espinet; M. Perez-Cadenas; A. Guerrero-Ruiz; I. Rodriguez-Ramos; P. Serp *Eur. J. Inor. Chem.* 2010, (32), 5096.
9. M. Woods; E. Biddinger; P. Matter; B. Mirkelamoglu; U. Ozkan *Catal. Lett.* 2010, **136** (1), 1.
10. D. von Deak; E. J. Biddinger; K. A. Luthman; U. S. Ozkan *Carbon* 2010, **48** (12), 3637.
11. S. van Dommele; K. de Jong; J. Bitter *Top. Catal.* 2009, **52** (11), 1575.
12. K. P. Gong; F. Du; Z. H. Xia; M. Durstock; L. M. Dai *Science* 2009, **323** (5915), 760.
13. C. Jin; T. C. Nagaiah; W. Xia; B. Spliethoff; S. Wang; M. Bron; W. Schuhmann; M. Muhler *Nanoscale* 2011, **2** (6), 981.
14. S. Kundu; W. Xia; W. Busser; M. Becker; D. A. Schmidt; M. Havenith; M. Muhler *Phys. Chem. Chem. Phys.* 2010, **12** (17), 4351.
15. S. Maldonado; K. J. Stevenson *J. Phys. Chem. B* 2005, **109** (10), 4707.
16. C. V. Rao; C. R. Cabrera; Y. Ishikawa *J. Phys. Chem. Lett.* 2010, 2622.
17. Y. Tang; B. L. Allen; D. R. Kauffman; A. Star *J. Amer. Chem. Soc.* 2009, **131** (37), 13200.
18. A. Cybulski; J. A. Moulijn *Catal. Rev. -Sci. Eng.* 1994, **36** (2), 179.
19. E. Garcia-Bordeje; I. Kvande; D. Chen; M. Ronning *Adv. Mater.* 2006, **18** (12), 1589.
20. S. Armenise; M. Nebra; E. García-Bordejé; A. Monzón *Stud. Surf. Sci. Catal.* 2010, **175**, 483.
21. Nijhuis TA; Beers AEW; Vergunst T; Hoek I; Kapteijn F; Moulijn JA *Catal. Rev-Sci. Eng.* 2001, **43** (4), 345.

22. N. Jarrah; J. van Ommen; L. Lefferts *Catal. today* 2003, **79–80**, 29.

23. W. Yang; T. P. Fellinger; M. Antonietti *J. Am. Chem. Soc.* 2010, **133** (2), 206.

24. D. Hulicova-Jurcakova; M. Kodama; S. Shiraishi; H. Hatori; Z. H. Zhu; G. Q. Lu *Adv. Funct. Mater.* 2009, **19** (11), 1800.

25. C. P. Ewels *J. nanosci. nanotech.* 2005, **5** (9), 1345.

26. M. Glerup *Chem. Commun.* 2003, (20), 2542.

27. Z. R. Ismagilov; A. E. Shalagina; O. Y. Podyacheva; A. V. Ischenko; L. S. Kibis; A. I. Boronin; Y. A. Chesalov; D. I. Kochubey; A. I. Romanenko; O. B. Anikeeva; T. I. Buryakov; E. N. Tkachev *Carbon* 2009, **47** (8), 1922.

28. T. Susi; A. Kaskela; Z. Zhu; P. Ayala; R. Arenal; Y. Tian; P. Laiho; J. Mali; A. G. Nasibulin; H. Jiang; G. Lanzani; O. Stephan; K. Laasonen; T. Pichler; A. Loiseau; E. I. Kauppinen *Chem. Mater.* 2011, **23** (8), 2201.

29. A. E. Shalagina; Z. R. Ismagilov; O. Y. Podyacheva; R. I. Kvon; V. A. Ushakov *Carbon* 2007, **45** (9), 1808.

30. T. Susi; G. Lanzani; A. G. Nasibulin; P. Ayala; T. Jiang; T. Bligaard; K. Laasonen; E. I. Kauppinen *Phys. Chem. Chem. Phys.* 2011, **13** (23), 11303.

31. J. Liu; S. Webster; D. L. Carroll *J. Phys. Chem. B* 2005, **109** (33), 15769.

32. S. Trasobares; O. Stephan; C. Colliex; W. K. Hsu; H. W. Kroto; D. R. M. Walton *J. Chem. Phys.* 2002, **116** (20), 8966.

33. Y. J. Cho; H. S. Kim; S. Y. Baik; Y. Myung; C. S. Jung; C. H. Kim; J. Park; H. S. Kang *J. Phys. Chem. C* 2011, **115** (9), 3737.

34. Q. H. Yang; P. X. Hou; M. Unno; S. Yamauchi; R. Saito; T. Kyotani *Nano Lett.* 2005, **5** (12), 2465.

35. F. Tuinstra; J. L. Koenig *J. Chem. Phys.* 1970, **53** (3), 1126.

36. J. Casanovas; J. M. Ricart; J. Rubio; F. Illas; J. M. Jiménez-Mateos *J. Am. Chem. Soc.* 1996, **118** (34), 8071.

37. P. H. Matter; L. Zhang; U. S. Ozkan *J. Catal.* 2006, **239** (1), 83.

38. J. R. Pels; F. Kapteijn; J. A. Moulijn; Q. Zhu; K. M. Thomas *Carbon* 1995, **33** (11), 1641.

39. E. Raymundo-Piñero; D. Cazorla-Amorós; A. Linares-Solano; J. Find; U. Wild; R. Schlögl *Carbon* 2002, **40** (4), 597.

40. G. S. Szymanski; T. Grzybek; H. Papp *Catal. Tod.* 2004, **90** (1-2), 51.

41. R. Schlögl; H. P. Boehm *Carbon* 1983, **21** (4), 345.

42. H. C. Choi; J. Park; B. Kim *J. Phys. Chem. B* 2005, **109** (10), 4333.

43. J. Lahaye; G. Nans; A. Bagreev; V. Strelko *Carbon* 1999, **37** (4), 585.

44. Z. Luo; S. Lim; Z. Tian; J. Shang; L. Lai; B. MacDonald; C. Fu; Z. Shen; T. Yu; J. Lin *J. Mater. Chem.* 2011, **21** (22), 8038.

45. H. Niwa; M. Kobayashi; K. Horiba; Y. Harada; M. Oshima; K. Terakura; T. Ikeda; Y. Koshigoe; J. i. Ozaki; S. Miyata; S. Ueda; Y. Yamashita; H. Yoshikawa; K. Kobayashi *J. Pow. Sour.* 2011, **196** (3), 1006.

46. R. A. Sidik; A. B. Anderson; N. P. Subramanian; S. P. Kumaraguru; B. N. Popov *J. Phys. Chem. B* 2006, **110** (4), 1787.